SAND2021-15177C

Joint Experimental/Computational Study of Fluid-Thermal-Structural Interaction of a Cone-Slice-Ramp in Hypersonic Flow

Aravinth Sadagopan* and Daning Huang†
Pennsylvania State University, University Park, PA, 16801

Adam Jirasek‡ and Jürgen Seidel§
United States Air Force Academy, Colorado, CO 80840

Anshuman Pandey¶ and Katya M. Casper‖
Sandia National Laboratories, Albuquerque, NM 87185

I. Introduction

Air-breathing hypersonic vehicles endure intense aerothermodynamic loading. As a consequence, the vehicle's structural characteristics and desired performance change during the flight. Moreover, the vehicle's weight constraint demands lighter and flexible control surfaces, and this makes the structure more susceptible to failure [1]. Studies in the past have relied upon simplified computational models to predict aerothermoelastic behavior. However, inherent approximations in these models led to inaccurate prediction of structural design margins [2, 3]. Another factor impeding progress was lack of high-resolution experimental data for numerical code validation [4–6]. Present shortcomings necessitate the usage of high-fidelity computational methods supplemented by high-resolution experimental data for a thorough understanding of the fluid-thermal-structural interaction (FTSI) behavior.

The present study focuses on a deflected ramp in a low Reynolds number inflow condition. Dominant flow features for this configuration can be identified by comparison with a laminar SWBLI using a canonical compression ramp. The relevant flow features include the separation shock, shear layer, separation bubble, reattachment shock, triple point, and reattachment streaks [4, 7, 8]. Experimental and numerical efforts have shown their interaction to manifest as low-frequency unsteadiness, for example as shear-layer flapping, Görtler-like vortices, etc. [9–12]. A significant factor governing the flow field is the ramp angle. For low ramp angles, SWBLI exhibits a two-dimensional behavior across the span. However, this pattern deviates at moderate and high ramp angles where flow features become three-dimensional. The complex flow feature interaction and resulting unsteadiness demand the usage of high-fidelity numerical methods for accurate aerodynamic assessment. Recent numerical and experimental efforts on flight-realistic geometries such as a cone-slice-ramp model [13–16] observed significant deviation from 2D compression ramp results, e.g. an arched shear layer impingement pattern on the ramp that lead to a span-wise variation in heat transfer and pressure distribution, three-dimensional nature of the separation bubble, and limited region of uniform flow on the ramp due to flow expansion effects on the span-wise edges.

The interplay of an oscillating impinging shock and a compliant cantilever panel was studied to simulate the fluid-structural interaction (FSI) of the control surface SWBLI problem by Currao et al. [17]. At $M_\infty = 5.8$, the laminar boundary layer separated and exhibited transition behavior due to the impinging shock. The occurrence of a turbulent boundary layer post reattachment was attributed to the Görtler instability. The wavelength of the Görtler vortices was independent of panel oscillations but its maximum amplitude disturbance depended on varying streamline curvature at reattachment. Peak pressure values were alleviated for the compliant panel case compared to the rigid case. Sullivan et al. [18] performed a two-dimensional direct numerical simulation on a 35° compression ramp because incipient laminar SWBLI formed a large separation bubble limiting the usage of analytical models for surface pressure evaluation. The fluid-structure interaction (FSI) analysis showed a reduction in the heat transfer rate for a compliant panel mounted to

*Ph.D. Candidate, Department of Aerospace Engineering, Student Member AIAA
†Assistant Professor, Department of Aerospace Engineering, Member AIAA
‡Senior Research Engineer, High Performance Computing Research Center, Senior Member AIAA
§Reasearch Director, High Performance Computing Research Center, Member AIAA
¶Postdoctoral Appointee, Engineering Sciences Center, Member AIAA
‖Principal Member of the Technical Staff, Engineering Sciences Center, Associate Fellow, AIAA

the ramp section compared to the rigid panel. The recent FTSI experimental effort by Pandey et al. [19] revealed a range of dominant frequency peaks for a large separated laminar SWBLI over the cone-slice-ramp (CSR) model. The dominant frequency peaks were associated with the unsteadiness in the separation shock and the shear layer. Thus, it is necessary to perform a numerical assessment to shed more light on the origin of unsteadiness.

Another characteristic feature of hypersonic flow is the existence of significant heat transfer rates that can modify the structural behavior. A heating experiment of rectangular panel by Freydin et al. [20] observed a shift in the panel's natural modal frequencies towards the lower end of the frequency spectrum with increasing temperature. Similar behavior was observed by FTSI experiments on compression-ramp model by Whalen et al. [21] and cone-slice-ramp geometry by Pandey et al. [19]. Accurately predicting this heat transfer is still a challenge for computational analysis given the time-scale disparity amongst fluid-thermal and fluid-structural interactions. A quasi-steady FTSI approach by Sadagopan et al. [22] overpredicted heat flux on the panel leading to the occurrence of thermal buckling. However, this behavior was absent in the experimental data. These studies indicate the need to calibrate structural model for modal content, and the fluid model for aero-thermal content that will eventually result into accurate FTSI predictions.

Recent datasets for FTSI validation include Vasconcelos et al. [23] on a clamped-free-clamped-free (CFCF) compliant panel at Mach 5.8, Riley et al. [6], and Spottswood et al. [5] on a flight-weight, realistic scale metallic flat panel mounted on a wedge at Mach 6 and 4, respectively. The aforementioned experimental dataset [23] compared a rigid panel and a compliant panel to isolate the effect of panel thickness and gross angle-of-attack on the aeroelastic response, as well was on the dominance of different aeroelastic mechanisms. It observed a transition from structure dominated response to a fluid dominated response resulting into a strong FSI coupling. In Ref. [6], the panel buckled in both directions and this effect was related to initial panel temperature, total pressure and location of the panel in the test section. Other observations included detection of local buckling and fixed-frequency oscillations of the panel. The Mach 4 inflow conditions in Ref. [5] generated laminar and turbulent boundary layer states on the panel. This study included a pre- and post- test analysis of the panel which observed only a slight difference in the modal content. However, the order of modes changed. A preheated thermal blanket was used to recreate a postbuckled state and the quasi-static aerothermoelastic behavior of this buckled panel was compared to a rigid predicted deformed panel. A dynamic snap-through was recorded when the panel shifted from a primary to a secondary equilibrium state at an inflow total temperature that is lower than the anticipated value. The later two studies involved usage of non-intrusive methods, such digital image correlation (DIC), Shack-Hartmann wavefront sensor (WFS), Forward looking infrared (FLIR), and high-speed Schlieren to detect FSI coupling. This highlights the need to perform a coupled FTSI analysis on flight-realistic models and inflow condition to understand the underlying physics.

The objective of the present work is to validate two computational frameworks for FTSI against experimental data to further the understanding of FTSI for a flight-realistic three-dimensional CSR. The specific objectives of this paper are listed as follows:

1. Validate two fluid solvers with experimental data.
2. Elucidate the complex flow physics of SWBLI for a cone-slice-ramp geometry.
3. Perform a quasi-steady FTSI analysis for the entire experimental runtime to understand the impact of simultaneous aerodynamic loading and heating on the structure.
4. Perform a transient FSI analysis for an unheated structure to understand the dynamic interplay of fluid and structure.
5. Identify the capabilities and limitations of computational FTSI analysis for high-speed applications.

II. Experimental Setup

A. Test Facilities and Test Conditions

Experimental measurements were carried out in the Sandia Hypersonic Wind Tunnel (HWT). It is a conventional blowdown-to-vacuum facility with an interchangeable system of nozzles and heater sections that allow either Mach 5,8, or 14 test conditions. In this work, the Mach 8 system was used which employs a bottle farm that stores Nitrogen (working fluid) at 689 MPa. A control valve between the high-pressure storage and the tunnel allows a $P_\circ$ range of $1720 - 6890$ kPa and an in-line heater provides a $T_\circ$ range of 500-890 K. This provides a Reynolds number (Re) range from $3.3 - 20 \times 10^6$ m^{-1} with a freestream noise level of 3-5% (Pitot pressure fluctuations divided by the mean Pitot pressure). The specific inflow conditions for the present study are given in Table 1.

Table 1 Wind-tunnel inflow condition for the present case

M_∞	Re (m^{-1})	$P_\circ$ (kPa)	$T_\circ$ (K)	Fluid	P_{cavity} (Pa)
8.0	4.0×10^6	2420	880	N_2	200

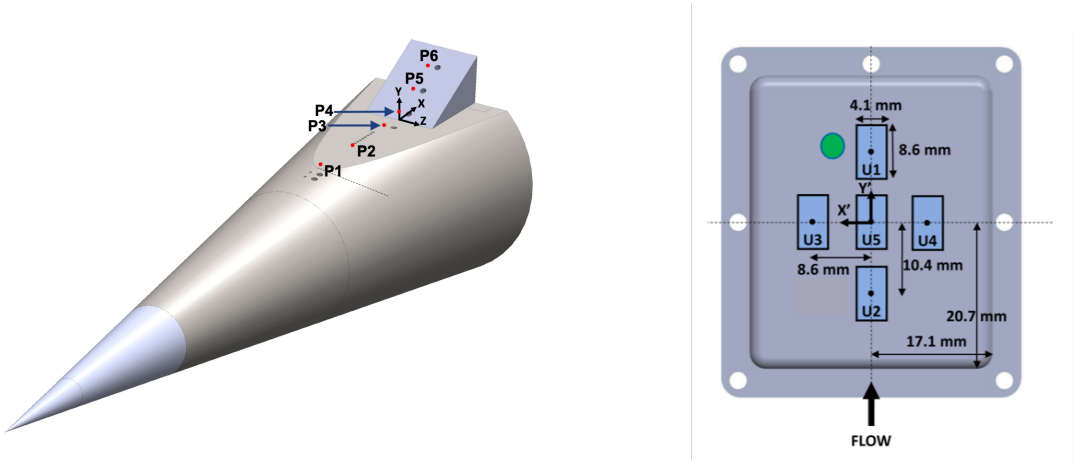

(a) Wind-tunnel test model with mounted panel representing a control flap; Red dots: Kulite sensors used for pressure correlation

(b) Backside of the panel describing the placement of accelerometer (U) and thermocouple (green dot)

Fig. 1 Experimental setup for the FTSI investigation of a cone-slice-ramp model

B. Model and Instrumentation

The study used a Joint Computational/Experimental Aerodynamics Program (JCEAP) [24] inspired geometry – a slender cone with a longitudinal slice at the aft-end of which a wedge-shaped control surface is placed to simulate a control flap as shown in Fig. 1(a). The stainless-steel model is a 7° half-angle slender cone with a base diameter of 127 mm. The wedge-shaped control surface is replaceable and a wedge angle of 30° is considered in this work. A solid wedge was used when pressure fluctuations were characterized on the surface while a hollow wedge was used for the FSI measurements that incorporated a thin panel on the front face of the wedge.

Multiple experimental campaigns with compatible flow interrogation techniques were carried out to obtain a qualitative and quantitative understanding of the flow-field. For the pressure measurements, transducers (Kulite Mic−062 or XCQ−30A) or high-frequency transducers (PCB132) have been used. These were mounted in two rows offset from the centerline as shown in Fig. 1(a). The exact location of the Kulite transducers used for validation of the computational models are provided in Table 2.

Table 2 Position of Kulite pressure sensors on the CSR model labeled in Fig. 1(a); $\theta = 30°$

Sensor code	x(mm)	y(mm)	z(mm)
$P1$	−88.0	0.0	−3.2
$P2$	−49.9	0.0	−3.2
$P3$	−11.8	0.0	−3.2
$P4$	$6.1\cos(\theta)$	$6.1\sin(\theta)$	−3.2
$P5$	$24.9\cos(\theta)$	$24.9\sin(\theta)$	−3.2
$P6$	$43.7\cos(\theta)$	$43.7\sin(\theta)$	−3.2

Surface heat flux measurements were carried out using temperature sensitive paint (TSP) and a reference heat flux sensor (MedTherm Schmidt-Boelter gauge) located at the PCB location 49.9 mm upstream of the corner. Oil flow

visualization of the surface streamlines was carried out using a thin layer of low viscosity fluorescent fluid (Zyglo ZL-27A). High framerate schlieren visualization was carried out using a high-speed pulsed laser (Cavilux Smart) and a high-speed camera (Phantom v2512).

FSI experiments used a hollow wedge with its front face formed by a thin panel (1mm thick) that responded to the unsteady fluid loading. For measuring the panel vibrations, five uni-axial accelerometers (PCB 352A73) were mounted on the back side of the thin panel, shown in Fig. 1(b). These accelerometers, that responded to the vibrations in the wall-normal direction to the panel, were placed such as to capture the first few natural modes of the panel. To obtain a-priori estimates of these modes, a hammer test was performed where complementary measurements using accelerometers and a Laser Doppler Vibrometry (LDV) system was carried out to measure the response of the whole cone to excitation by a calibrated impact hammer. By design, the panel structural modes were at higher frequencies than those of the cone-wedge body holding the panel and the sting mount used to mount the cone in the wind tunnel. Two type-T thermocouples were used on the panel and the wedge frame to obtain the temperatures of the thin panel and its boundary conditions, respectively. The thermocouple on the panel was located near the top accelerometer (shown in Fig. 1(b)) and RTV was used to paste the frame thermocouple. Further details on the experimental techniques and the data acquisition methods can be obtained in previous works [14, 19].

III. Computational Modeling and Validation

In this study, two computational frameworks are considered. Framework 1 is developed recently at the Pennsylvania State University (PSU), and Framework 2 is from the US Air Force Academy (USAFA). The details of these two frameworks, as well as the computational models for the cone-slice-ramp geometry, are discussed.

A. General Strategy for Coupled FTSI Analysis

The computational frameworks in the present study both employ a partition-based approach for the coupled analysis, i.e. using separate solvers for different physical domains. The validity of this approach relies on the time scale disparity amongst the individual physical domains in hypersonic flows [3, 25]. To verify the disparity for the present problem, the aerothermal and aeroelastic characteristic times are estimated.

The aerothermal characteristic time is determined by the Fourier number,

$$t_{AT} = \frac{\rho^s {c_p}^s h^2}{k^s} \tag{1}$$

where ρ^s is solid panel density, c_p is solid specific heat capacity, h is the thickness and k^s is solid thermal conductivity.

The aeroelastic characteristic time is determined by the fundamental structural frequency f_1,

$$t_{AE} = \frac{1}{f_1} \tag{2}$$

In the current problem, $t_{AT} = 0.256$s and $t_{AE} = 1.8 \times 10^{-4}$s. The three orders of magnitude difference between t_{AT} and t_{AE} allows us to decouple the FTSI problem into two parts:

1. Quasi-steady FTSI response that involves the conjugate heat transfer of the structural model and the static thermally-induced structural deformations.

2. Transient FSI response that involves the time-resolved structural responses and ignores the time variation in the temperature distribution.

The quasi-steady FTSI analysis is performed over the entire period of experiment with a large time step size on the order of t_{AT}, while the transient FSI analysis is performed over a select short time period with a small time step size on the order of t_{AE}. In both cases, the analysis may be completed within $10^3 - 10^5$ steps and thus is computationally tractable. In this study, the FSI analysis is performed at $t = 0$s, i.e. when the panel is still unheated.

B. PSU Framework

1. Computational Fluid Dynamics

The SWBLI is resolved using STARCCM+®, a numerical finite volume code where the conservation equations are solved simultaneously as a vector of equations, velocity, pressure and density are obtained from the momentum

equation, continuity equation and equation of state, respectively.

$$\frac{\partial}{\partial t}\int_v \mathbf{W}dv + \oint [\mathbf{F}-\mathbf{G}].da = \int_v \mathbf{H}dv \tag{3}$$

where,

$$\mathbf{W} = \begin{bmatrix} \rho \\ \rho\mathbf{v} \\ \rho(H - p/\rho) \end{bmatrix}, \quad \mathbf{F} = \begin{bmatrix} \rho\mathbf{v} \\ \rho\mathbf{v}\mathbf{v} + p\mathbf{I} \\ \rho\mathbf{v}H + p\mathbf{v} \end{bmatrix}, \quad \mathbf{G} = \begin{bmatrix} 0 \\ \mathbf{T} \\ \mathbf{T}.\mathbf{v} + \dot{q} \end{bmatrix}$$

where, the enthalpy $H = c_pT + |\mathbf{v}|^2$, $\mathbf{W}$ is the inertial term, $\mathbf{F}$ and $\mathbf{G}$ correspond to convective and diffusive fluxes and $\mathbf{H}$ is the vector of sources and body forces. Discretized convective fluxes are solved using hybrid MUSCL (Monotone Upstream-centered Scheme for Conservation Laws) third-order central difference scheme. It has the ability to control numerical dissipation by switching to a first-order scheme in the vicinity of shocks. In regions of high Mach number, the flux value is reconstructed using WENO (Weighted Essentially Non-Oscillatory) schemes to minimize non-physical oscillations. The inviscid flux component is resolved with AUSM+ (Advection Upstream Splitting Method) flux vector splitting scheme. Gradients are computed using hybrid gauss-least squares method.

The discretized system of Eq. (3) is solved using an algebraic multi-grid method which is faster than conventional iterative solution algorithms. A multi-grid method reduces low-frequency errors through an iterative process on a hierarchy of successively coarsened linear systems. In the present implementation, a Gauss-Seidel iteration scheme is accelerated by the algebraic multigrid cycling method. Additional linear solver acceleration at each level is carried out using Bi Conjugate Gradient Stabilized method. A laminar flow solver is used as the present study involves a low Reynolds number inflow condition. Since, no turbulence modeling is involved, this is a direct approach where the numerical solver is equivalent to an implicit large eddy simulation (ILES) method. Therefore, the solution accuracy is proportional to the grid resolution. The ideal gas law is used to model equation of state as the compressibility factor did not vary significantly for both the cases considered. Dynamic viscosity is modelled using Keyes law given in Eq. (4) for low static temperature values where viscosity deviates from Sutherland's law.

$$\mu(T) = \frac{1.488 \times \sqrt{T}}{1 + (122.1/T) \times 10^{-5/T}} \tag{4}$$

The thermal conductivity is modelled with Sutherland's law given in Eq. (5).

$$\frac{k(T)}{k_0} = \frac{T}{T_0}^{3/2} \frac{T_0 + S}{T + S} \tag{5}$$

where reference temperature $T_0 = 273.15$K, reference conductivity $k_0 = 0.02414$W/mK, and Sutherland's constant $S = 194$K.

2. Computational Thermo-Structural Dynamics

The FTSI method implements the finite volume stress model in STAR-CCM+®. The main advantage of using the finite volume solid stress is that it makes it possible to simulate FTSI completely within the framework of STAR-CCM+®, and minimize the computational overhead due to the coupling between different solvers. It uses a Lagrangian approach to calculate the temperature field, displacement field and its motion is governed by the conservation of linear momentum (Cauchy's equilibrium equation), in Eqs. (6) and (7).

$$\int_V \rho\ddot{\mathbf{u}}\, dV = \int_A \vec{\sigma} \cdot d\,\text{v.s.} + \int_V \mathbf{b}\, dV \tag{6}$$

$$\int_V \rho C_p \dot{T}\, dV = \int_A \mathbf{q} \cdot d\,\text{v.s.} + \int_V s\, dV \tag{7}$$

where,

$$\rho(\vec{\sigma}, T) = \rho_o(1 - \alpha(T - T_{ref}) - \frac{\vec{\sigma}}{K})$$

$$\vec{\sigma} = f(\vec{\epsilon}, T)$$

T is the temperature, $\mathbf{u}$ is the displacement field, $\vec{\sigma}$ is the stress tensor, $\vec{\epsilon}$ is the strain tensor $\mathbf{q}$ is the heat flux, $\mathbf{b}$ represents the body force, and s is the heat source. The momentum equation Eq. (6) and Eq. (7) are discretized into a residual form given in Eq. (8). For the structural solver, the acceleration and velocity components are approximated using 2^{nd} order Newmark β method which estimates velocity and position at every time step.

$$\dot{\mathbf{u}}^n = \dot{\mathbf{u}}^{n-1} + (\gamma\ddot{\mathbf{u}}^n + (1-\gamma)\ddot{\mathbf{u}}^{n-1})\Delta t \tag{8}$$

$$\mathbf{u}^n = \mathbf{u}^{n-1} + \dot{\mathbf{u}}^{n-1}\Delta t + (\beta\ddot{\mathbf{u}}^n + (0.5-\beta)\ddot{\mathbf{u}}^n)\Delta t^2 \tag{9}$$

Choosing $\gamma = 1/2$ and $\beta = 1/4$ renders the numerical method second-order time accurate and stable for linear systems.

3. Computational Domain

To minimize computational cost, the 3D CSR fluid domain is truncated in the streamwise and azimuthal direction retaining the aft-section after $x = 342$ mm along with a 120° section of the top-half, as shown in Fig. 2(a). The truncated domain is prescribed with a steady inflow condition obtained from an axisymmetric precursor simulation. The fluid domain size is $L_x \times \frac{2}{3}(L_{r,in} \rightarrow L_{r,out}) = 175.8$ mm$\times\frac{2}{3}\pi(41.91, 56.80 \rightarrow 63.5, 106.78)$ mm. A multi-block structured mesh is used to discretize this fluid volume. In the azimuthal direction, $\Delta z^+ = 8.1$ is over the slice and $\Delta z^+ = 121$ near the periodic boundaries. The streamwise direction values are $\Delta x^+ = 12$ near the inflow boundary, $\Delta x^+ = 5$ on the slice and $\Delta x^+ = 30$ near reattachment on the ramp section. The first wall-normal grid resolution varies from $\Delta y^+ = 0.2, 0.25$ in the inflow and the separation bubble to $\Delta y^+ = 1.35$ post shear layer reattachment near the outflow. The grid resolution inside the separation bubble is maintained around $\Delta y^+ = 6$. Overall, the grid is discretized as $N_x = 650$, $N_y = 150$, $N_z = 240$ (~ 25.34 million cells). An illustration of this mesh across the spanwise center-plane of CSR is given in Fig. 2(b). The 'cone-slice-ramp' term in the subsequent discussion refers to the aft section of the cone-slice-ramp model downstream of $x = 340$ mm.

The CSR structure is simplified to a solid rectangular panel underneath the wedge surface for FTSI analysis. It has been established in previous work [22] that modeling the panel alone shall suffice for FTSI. The material is assumed to be linear isotropic elastic and its properties are given in Table 3. Geometrically, the solid panel's top surface exactly coincides with the panel boundary highlighted in Fig. 2(a). The side walls of the solid panel are specified as clamped boundary condition. The effect of accelerometer and thermocouple sensors is found to be significant while evaluating the panel's natural frequencies. The solid panel is discretized using a finite volume mesh with ($N_\eta \times N_\xi \times N_z = 150 \times 10 \times 100$) 150000 cells. The geometric definition of the solid panel along with sensors is given in Fig. 1(b). A comparative assessment of the structure's natural frequencies is given in Table 4. The panel back-pressure (cavity pressure) is prescribed a constant value of 200 Pa based on the experiment. The back surface of the panel is assumed to be insulated. For experiment considered in this study, the surfaces of the rigid mounting frame is specified to be isothermal with $T_w = 308.0$ K. The panel is initialized with zero displacement and a constant temperature, $T_w = 333.0$ K based on the initial condition in the experiment. The isothermal wall assumption for the mounting frame is reasonable, as the temperature rise in the frame is not significant, based on the experimental results. However, the isothermal boundary condition does result in a heat sink capability that is higher than the actual structure.

4. Coupled FTSI Analysis

The quasi-steady FTSI analysis is performed over the entire duration of the experiment. The quasi-steady analysis employs a large time step size that is comparable to the thermal characteristic time, and neglects the high frequency oscillations of the structure. In the quasi-steady FTSI analysis, the fluid solver advances the solution in a quasi-steady manner with 150 iterations for every time step of the thermo-structural solver at $\Delta t = 0.1s$ with 100 iterations. The prescribed coupling time step is lower than the aerothermal characteristic time $t_{AT} = 0.256s$. All the thermo-structural computations are carried out over the solid panel. The fluid solver leads the solution at every thermo-structural time step. In terms of data exchanged, the fluid solver transfers pressure, wall shear stress and heat flux information to the thermo-structural solver. After propagating the solution for $\Delta t = 0.1s$, the thermo-structural solver sends displacement and wall temperature information back to the fluid solver.

The transient FSI analysis is performed over a time period of 10^{-3} second. The transient analysis fully resolves the structural dynamic response, but ignores the variation in structural temperature due to the short time frame. The transient

Table 3 Material property of the cone-slice-ramp test structure (Stainless steel)

E (GPa)	ρ (Kg m^{-3})	μ	α (K^{-1})	c_v (JK Kg^{-1})	k (WK m^{-1})
200	8060	0.3	1.3×10^{-5}	466.0	14.4

FSI is performed using solvers that propagate and exchange information explicitly at a time step of $\Delta t = 2.5 \times 10^{-6}$ s. The time step size allows for a resolution of 24 time steps for every period of the fourth natural mode having a frequency of 17.5 kHz. In terms of solver sequencing and data exchange across the fluid-solid interface, pressure and wall shear stress information is transferred from fluid solver to structural solver. After each time step, the computed displacement is transferred back from structural to fluid solver.

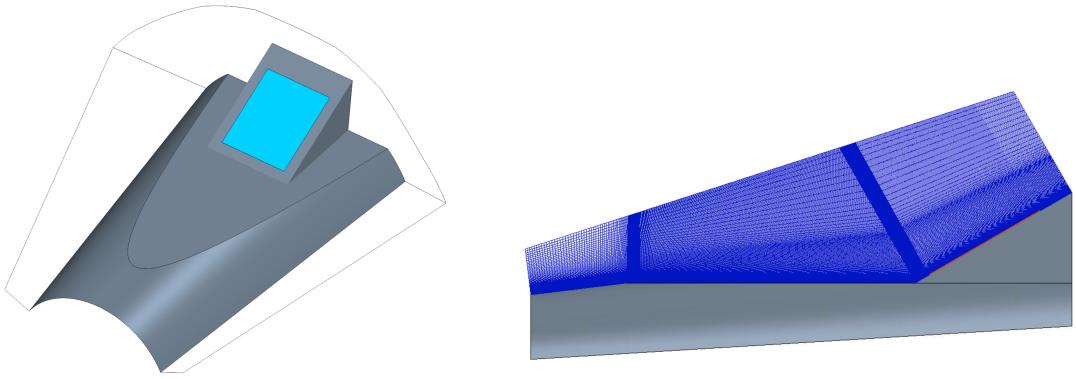

(a) Truncated computational fluid domain of the CSR model **(b) Detail of the mesh across the center-plane of CSR (highlighted red line on the wedge represents the panel**

Fig. 2 Computational mesh used for CFD in the PSU Framework

C. USAFA Framework

1. Overview of Solvers

The USAFA Framework is based on the code Loci/CHEM, a CFD solver developed at the Mississippi State University by Luke et al.[26, 27]. It uses a finite volume scheme with inviscid fluxes calculated using the HLLC inviscid flux scheme by Torro [28]. A low dissipation upwind scheme is also available. The time integration scheme uses a second order Newton implicit scheme. The solver can be used with moving, deforming and overset meshes.

The solver uses a rule based programming framework called Loci [29–31]. The solver consists of a set of rules which are scheduled in the Loci framework during execution. Loci takes care of scheduling as well as MPI partitions transfer. This approach simplifies the design of high performance parallel codes. The coding is in the Loci language which during compilation is converted into C++ code and compiled to executable.

The solver is distributed by the Mississippi State University and the distribution of the solver is ITAR compliant.

The coupling to an external solver is done through TCP/IP library [32]. The structural code used in this study is a modal solver which uses backward Euler time integration scheme. The coupling to the structural code is done at every subiteration level. The structural modal data is obtained experimentally or precomputed in a modal analysis step, which will be discussed in the later sections.

The fluid-thermal interaction uses coupling of Loci/CHEM and Loci/Heat. Loci/Heat is a finite volume solver using the same numerical scheme as Loci/CHEM CFD solver. It is delivered as a part of Loci/CHEM distribution. The original version however needed some updates into the source code since the original implementation would not allow running the heat solver as a standalone code. In addition, the solver required implementation of the same TCP/IP communication mechanism used in Loci/CHEM so that both solvers can be coupled.

2. Computational Domain

The mesh for the fluid domain is made in Pointwise and uses prism layer on the surface with $y^+ < 1$ and growth ratio 1.1, as shown in Fig. 3. In addition to that the mesh contains blocks of refined structured mesh around shock waves and in the wake to improve shock and expansion wave resolution. This case uses Nitrogen as working gas and the flow is considered laminar.

The mesh of the structure is also made in Pointwise. The surface mesh on the surfaces which are in contact with air are point matched meshes; the heat flux and temperature transfer are not interpolated during the transfer from CFD to the Heat solver and vice versa. The mesh has a prism layer similar to the CFD mesh. The initial spacing is 0.1 mm growth ratio is 1.1. The mesh allows heat transfer from the panel and rest of the body through the bottom part of the panel, there is a small gap on each side of the panel (shown in Fig. 4(c)) which does not permit heat transfer between the panel and the rest of the model. This is because no substantial contact is expected there as the experiment did not detect the buckling of the panel. The model material is steel.

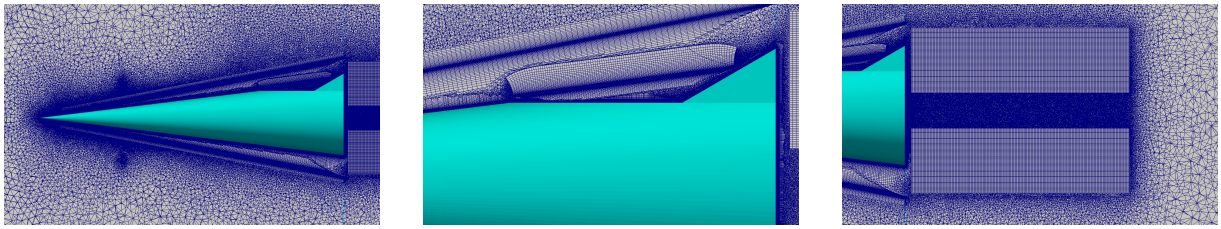

(a) Computational mesh in the vicinity of the cone **(b) Detail of the mesh around panel** **(c) Detail of mesh behind model**

Fig. 3 Computational mesh used for CFD in the USAFA Framework

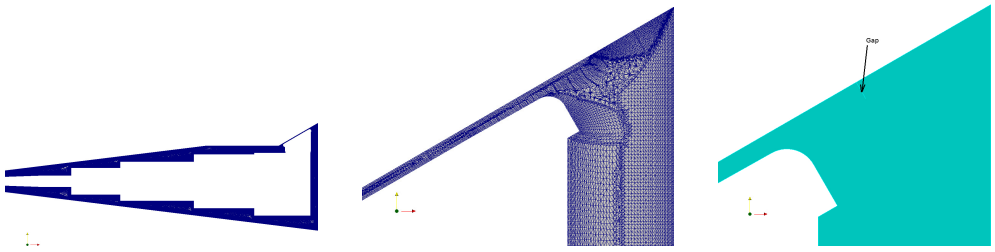

(a) Cut through the material **(b) Detail of the mesh around panel** **(c) Gap in the mesh**

Fig. 4 Computational mesh used for heat transfer analysis in the USAFA Framework

3. Coupled FTSI Analysis

The transient FSI analysis employs the structural modes provided by Sandia National Lab generated by structural hammer testing prior to the wind-tunnel campaign. The modes were projected onto the CFD mesh using Radial Basis Functions (RBF). Again the steel is considered as the material for which 109 modes are available from the hammer test data. The damping coefficients identified from the test are retained in the modal solver. The time step used for FSI analysis is $\Delta t = 1 \times 10^{-6} s$. As mentioned earlier, the coupling is done at every subiteration level and for this problem we use 5 Newton sub-iterations. At the beginning, the modes are excited by an initial pulse.

The quasi-steady FTSI analysis is performed in a loosely-coupled manner, consisting of three sequential steps: FTI analysis, modal analysis, and FSI analysis. This sequential strategy is valid if the structural deformation is sufficiently small and does not impact the aerodynamic loading and heating. First, FTI analysis of the entire model, where the structure is assumed to be rigid, is performed over the duration of the experiment. A time step size $\Delta t = 0.01 s$ and 6 Newton subiterations are used for the FTI analysis. From the FTI analysis one obtains the time-dependent temperature distribution in the structure. Subsequently, the temperature distributions, sampled using a step size of $1 s$, is provided to

a modal analysis code to produce the structural modes of the heated panel. Interpolating the structural modes at different time steps, one obtains the structural modes at any time step. Finally, the time-dependent temperature distributions and structural modes are provided to the FSI analysis for a new FSI solution over the experiment duration. In this process, a large time step size is employed and critical damping coefficients are assumed for each mode, so that the structural response do not admit oscillations. As a result, the FSI solution approximates the quasi-steady FTSI solution.

D. Calibration of the Structural Model

In the previous experimental study [19], some discrepancies are observed in the modal data obtained from the hammer test, spectral proper orthogonal decomposition (SPOD) analysis of the experimental data, and the theoretical modal solutions of a fully-clamped panel. Such discrepancies are shown in the first three columns of Table 4. In particular, note that the fundamental frequency found in the experiment is lower than the theoretical solution. For the successful correlation between the experimental and computational results, the numerical model of the structure requires a careful calibration.

First of all, there was a change in the sensor configuration on the panel between the hammer test and the wind tunnel test. The changes in sensor alters the total mass and mass distribution of the panel. As a result, the hammer test data and the SPOD data are expected to differ. In addition, the SPOD analysis is performed using sensors that are sparsely placed on the panel, and therefore the modal data may not be accurate. The experimental measurement for the modal data is expected to improve when digital image correlation data becomes available.

Next, comparing the theoretical and experimental results, there are two possible sources of discrepancies: imperfect boundary conditions (BCs) and the added mass due to the sensors. The theoretical solution considers only the thin panel section, while the experiments are based on the entire structure, involving the mounting frame. The leading edge of the mounting frame is not bolted as its other three edges, so as to avoid disturbance of the flow downstream on the panel. Such relaxed constraint may lead to imperfect clamped BC, and hence reduced structural stiffness and natural frequencies. On the other hand, the sensor mass increases the total structural mass, which may also lead to reduced natural frequencies, even if the panel is fully clamped.

Two structural models are considered to analyze the sources of discrepancies. The first model is based on the Rayleigh Ritz (RR) method, where springs on the edges of panel are used to represent imperfect BCs and point masses are used to represent the sensors. The theoretical formulation of the RR method is provided in Appendix A. The second model is a detailed 3D finite element model of the panel using the commercial software ABAQUS, with the sensors modeled as blocks of masses.

The 4th-6th columns in Table 4 show that it is possible to match the structural frequency with the experimental data by making the leading edge of the panel simply supported or spring constrained. The last two columns in Table 4, however, show that adding the sensor masses also leads to properly tuned structural model, without tuning the boundary conditions. On the other hand, the total added mass is expected to be $\sim$10% of the panel mass, and therefore is considered to be the main factor causing the discrepancies in the frequencies, instead of the imperfect BCs. In addition, the mode shapes predicted by the RR method are compared for the effect of sensor mass in Fig. 5. The masses alter not only the frequencies, but also the order of mode shapes, e.g. modes 4 and 5, 8 and 9, 10 and 11.

Finally, the calibrated 3D structural model (yellow column in Table 4) with sensor masses is used in the FSI and FTSI analysis of PSU Framework, while the RR-based structural model with point masses (orange column in Table 4) is used to generate the modal data for the FTSI analysis of USAFA Framework.

E. Aerodynamics for the Rigid-Wall Case

The time-averaged surface pressure is evaluated on the CSR model along a line oriented in the stream-wise direction. An offset of $z/L = -0.0342$ (span-wise direction) is applied throughout the line to match the experimental probe location. All the length units are non-dimensionalized using a reference length, $L = 0.0931$ m (slice length). The numerical predictions are compared across sensors spanning upstream of cone-slice junction located at $x/L = -1$ to ramp section from $x/L = 0$ to $x/L = 0.5$ as illustrated in Fig. 6. The comparison highlights the computational accuracy of both the frameworks by showing a good match with the experimental data. A slight offset is observed for the last sensor located at $x/L = 0.4$.

The numerically predicted flow features are evaluated against the time-averaged experimental schlieren image along the spanwise center-plane in Fig. 7. White indicates region with high density gradient. All the major flow features are accurately predicted in both the numerical frameworks which include separation shock, shear layer, reattachment shock and separation bubble. The predicted mean wall shear stress magnitude over the cone-slice-ramp are compared to

Table 4 Comparison of panel frequencies: T-Theory [19], E-Experiment [19], N-Numerical; C-Clamped, S-Simply supported. (All the values are in kHz)

	E(Hammer)	E(SPOD)	T	N(FEM)	N(FEM)	RR	RR	N(FEM)
BC			CCCC	CCCC	CCCS	Tuned	CCCC	CCCC
Sensor mass	*Yes*	*Yes*	*No*	*No*	*No*	*No*	*Yes*	*Yes*
Mode (1,1)	5.4	5.6	6.2	6.13	5.73	5.47	5.84	5.85
Mode (1,2)	9.8	10.3	11.1	10.96	9.79	9.64	9.71	10.53
Mode (2,1)	9.3	12.7	13.9	13.75	13.68	12.82	12.09	13.21
Mode (2,2)	20.2	-	18.5	17.96	16.85	16.76	14.19	17.68
Mode (1,3)	16.4	16.2	19.1	18.144	17.45	16.69	16.67	17.8

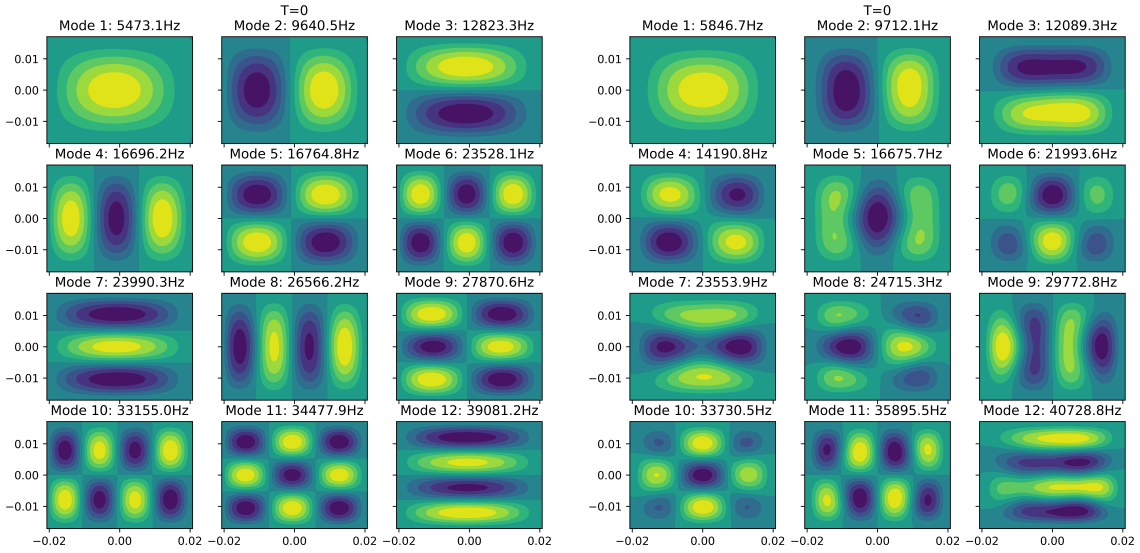

(a) without the sensors **(b) with the sensors**

Fig. 5 Mode shape and frequency predicted by the Rayleigh-Ritz method for an unheated and undeformed panel; x-axis: Length of the panel, *a*; y-axis: Width of the panel, *b*

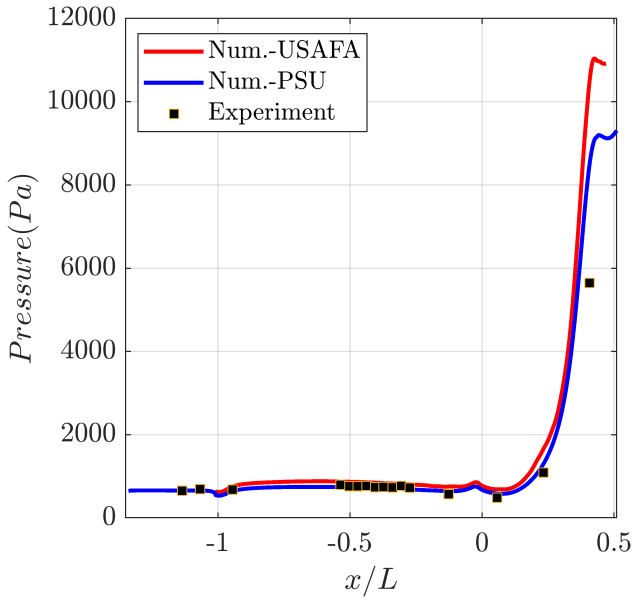

Fig. 6 Comparison of the time-averaged pressure data along a line ($z/L = -0.0342$) on cone-slice-ramp model

an oil flow visualization from the experiment, shown in Fig. 8. White and black regions indicate low and high shear stress values. Figure 9 shows the comparison of experimental heat transfer with numerical predictions using Stanton number. The overall comparison for both the quantities show a good match between the numerical frameworks and the experiment. The location of shear layer separation is identified with reduced heat transfer around the cone-slice junction. The same behavior is visible in the wall shear stress contours. Two flow structures, corner vortex (originates from wedge-slice corner) and horse-shoe vortex (originates from cone-slice corner flow separation) are present on the slice section. The location of these features are identical to another low Reynolds number CSR case at Mach 5 [14]. One can also observe from the heat transfer and wall shear stress data that the upstream laminar boundary layer continues to be laminar along the cone surface. Unlike the 2D compression ramp results of Cao et al. [9], shear layer impingement displays an arched pattern as evident in the heat transfer contours of Fig. 9. It indicates a three-dimensional flow reattachment pattern present in a flight-realistic geometry.

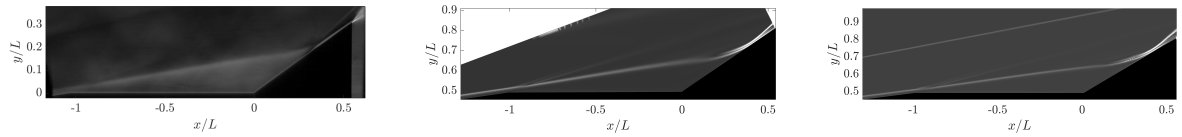

(a) Experiment **(b) Numerical - PSU** **(c) Numerical - USAFA**

Fig. 7 Comparison of time-averaged Schlieren images at the centerplane of cone-slice-ramp model at M_∞ = 8

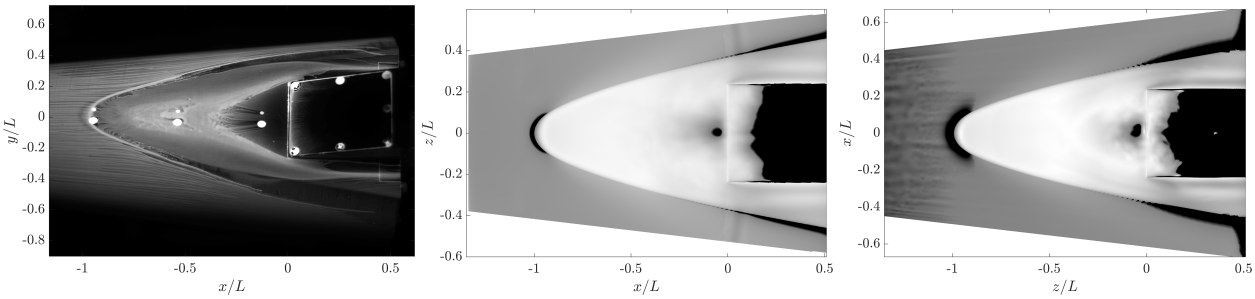

(a) Experiment (Oil flow visualization) (b) Numerical - PSU (c) Numerical - USAFA

Fig. 8 Comparison of wall shear stress on the cone-slice-ramp model at M_∞ = 8

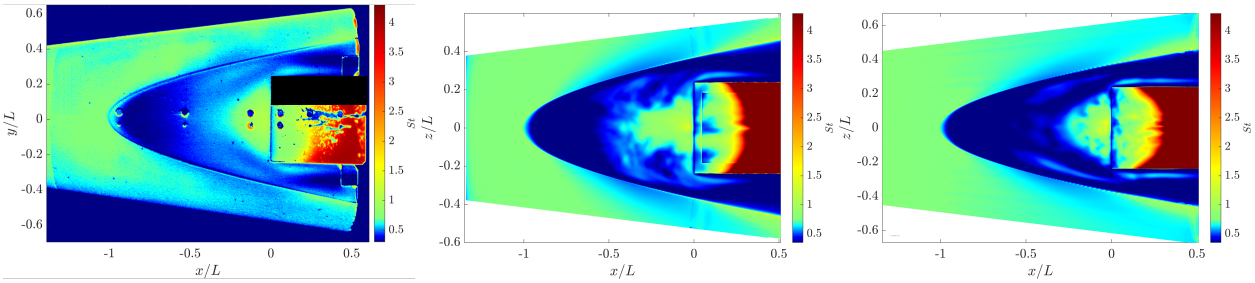

(a) Experiment (TSP) (b) Numerical - PSU (c) Numerical - USAFA

Fig. 9 Comparison of wall heat flux on the cone-slice-ramp model at M_∞ = 8; Stanton number = St$\times 10^3$

The unsteady pressure is compared at three locations on the cone-slice-ramp model using power spectral density (PSD) spectrum as shown in Fig. 10. These pressure sensors are highlighted in Fig. 1(a). Sensor 'P1' is located just downstream of the cone-slice junction within the separation bubble. Figure 10(a) shows a prominent peak in the experimental data at 1.4 kHz and both the numerical frameworks predict it accurately. This behavior is associated with the low-frequency oscillation [4] of the separation bubble. This same frequency is also associated with a structural natural frequency of the cone-sting body [19]. It has yet to be determined if the aerodynamic phenomena at this frequency and the structural mode at the same frequency are coupled. Sensor 'P5' located at the center of the panel lies just upstream of the shear layer reattachment. The experimental PSD in Fig. 10(b) shows a broad peak at 17 kHz related to the shear layer flapping phenomena as discussed in [19]. The PSU framework predicts this unsteady flow feature. Lastly, unsteady data at the post-reattachment region is compared with sensor 'P6' located at the aft end of the ramp section. The experimental PSD plot in Fig. 10(c) shows a broadband spectrum highlighting transition to turbulence [4, 10]. The PSD of both the numerical frameworks at 'P6' display similar behavior. It is important to note that the PSU numerical model implements a uniform laminar inflow condition simulating only the aft section of the CSR model and the USAFA framework resolves the flow field over the complete CSR model.

The vortical structures generated by the cone-slice-ramp geometry are visualized using the Q-criterion with a value of 9×10^9 (s^{-2}) as shown in Fig. 11(a) and Fig. 11(b). This value is chosen to highlight the distinct flow structures present in this flow field. Figure 11(a) is annotated to highlight these structures. First, the separation shock generates a horse-shoe vortex which travels downstream on the slice section. This is also seen in heat transfer contours of Fig. 9(a). The second and third labels correspond to the upstream and downstream legs of the streamwise vortices triggered due to a combination of secondary instabilities in the shear layer [33] and the curvature of shear layer near reattachment [9, 17]. The upstream leg of the streamwise vortex interacts with the separation bubble present over the slice-ramp section and disintegrates. This behavior is distinctively different from the low Reynolds number computational result by Thome et al. [15] for a 20° cone-slice-ramp model. The corner vortices shed from the wedge-slice spanwise edge is highlighted as well. The same set of flow structures are observed in the USAFA Framework as shown in Fig. 11(b).

The predicted time-averaged and time-resolved data reasonably match with the experimental data. It validates the accuracy of fluid solvers in both the numerical frameworks. Further, predicted mean flow features compare well with

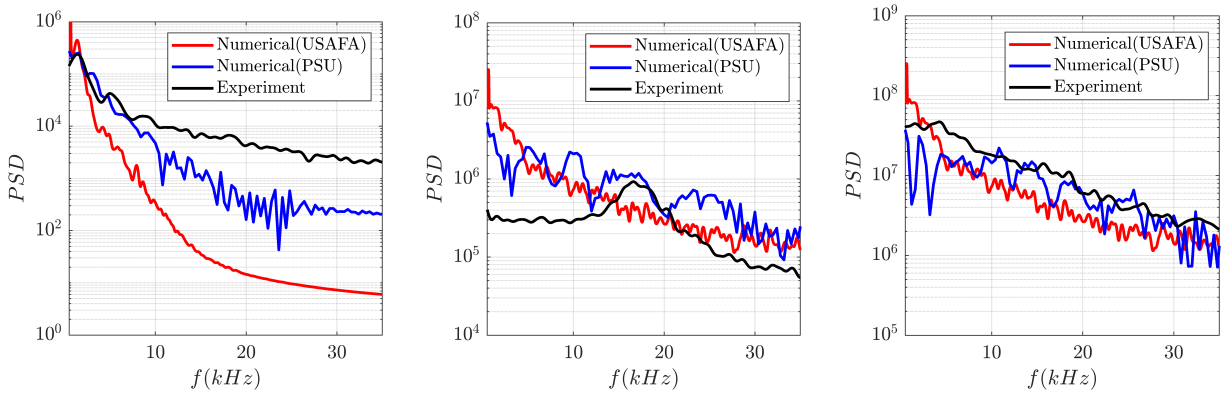

(a) PSD at 'P1' (b) PSD at 'P5' (c) PSD at 'P6'

Fig. 10 Comparison of unsteady pressure data obtained from numerical methods compared against experimental data using power spectral density (PSD) spectrum. Probe locations highlighted in Fig. 1(a)

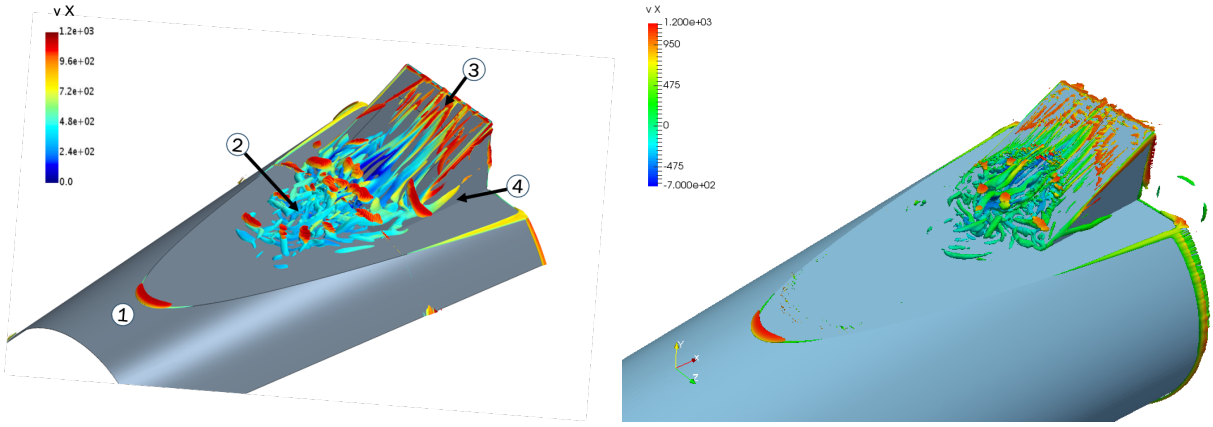

(a) Numerical-PSU (b) Numerical - USAFA

Fig. 11 Instantaneous snapshot visualized using Q-criterion isosurfaces, where the structures are highlighted with the stream-wise velocity component

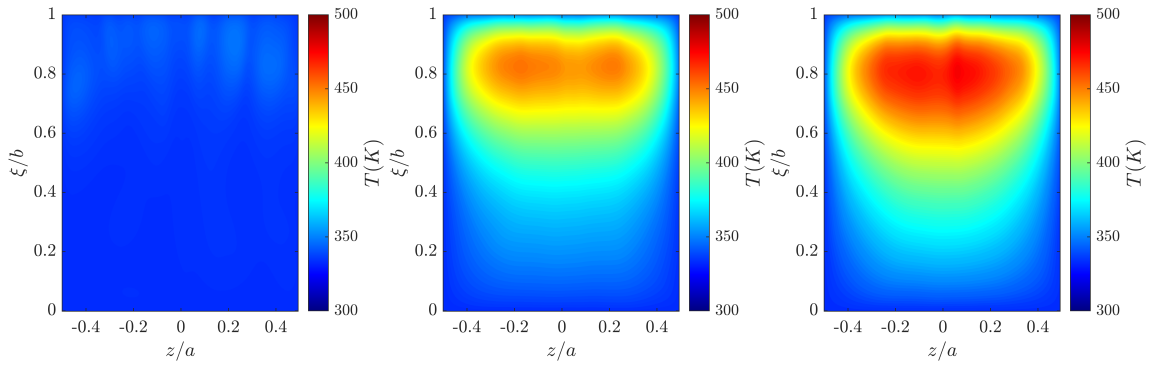

(a) t=1s **(b) t=30s** **(c) t=50s**

Fig. 12 Change in wall temperature (T) due to panel heating, where a,b are the panel dimensions. Flow direction is from bottom ($\xi/b = 0$) to top ($\xi/b = 1$)

the experimentally observed flow features providing confidence in the usage of high-fidelity numerical fluid solvers for the FTSI study.

IV. Quasi-Steady Fluid-Thermal-Structural Interaction

The fluid-thermal-structural interaction (FTSI) results predicted from both the computational frameworks are presented in this section.Further, a detailed discussion is given on the changing modal characteristics of the panel (control surface) when subjected to the heat load of a large separated laminar SWBLI for a long duration of a minute.

A. Correlation to the Experimental Results

1. PSU Framework

The temperature rise (T_w) on the top wall of the compliant panel is visualized in Fig. 12 for three discrete time steps. All length units are non-dimensionalized with a (length) and b (width) of the panel. At $t = 1$s in Fig. 12(a), the imprints of streamwise vortices are visible locally ($\xi/b > 0.7$) in the temperature distribution. They act as the singular heating source as evident in all the temperature contours up to $t = 50$s. Though these vortices exist throughout the span (z/a), temperature rise is concentrated in the central region ($z/a = -0.4$ to 0.4). This occurs due to a simplification made in the structural model. Only the panel is considered for structural response (discussion in sec. III.B.2) and its side walls are prescribed with an isothermal boundary condition of $T_w = 333$K. At the end of $t = 50$s, the panel locally heats up to $480K$ in the region corresponding to streamwise vortices.

The temperature rise of the panel is presented for the five sensor locations 'U1' to 'U5' in Fig. 12. Wall temperature (T_w) at 'U1' (top section of the panel) has the highest magnitude as it lies in the vicinity of the streamwise vortices. At the end of $t = 50$s, $\Delta T_w = 137$K at 'U1', but the slope reduces due to a reduction in the heat flux. Comparing this trend to 'U2' located beneath the separation bubble, the temperature rise is linear with a $\Delta T_w = 40$K at the end of $t = 50s$. The other three sensors 'U3', 'U5' and 'U4' are located in the central section of the panel at span $z/a = -0.3, 0.0, 0.3$. The heat flux is symmetric across the centerline ($z/a = 0$) as 'U3' and 'U4' have overlapping T_w curves with a $\Delta T_w = 40$K at the end of $t = 50$s. The T_w curves highlight a non-uniform temperature rise across the panel due to localized heating of streamwise vortices.

The temperature rise data is compared against the thermocouple data of the experiment at $\xi/b = 0.8, z/a = 0.1$ in Fig. 14(a). An excellent match is observed validating the present numerical framework by coupling a quasi-steady fluid solver to the thermo-structural solver leveraging on the time-scale disparity concept. Another advantage of this method is that it allows for studying FTSI response beyond the experimental run-time limitations.

The corresponding transverse displacement (u_η) of the panel is visualized in Fig. 13 at the same time steps. As temperature increases, the fore section of the panel subjected to lower temperature bends away from the flow. This occurs due to the dominance top wall's high pressure values over the bottom wall's lower cavity pressure. However, the aft section (20% of the panel chord) subjected to the intense heating of the streamwise vortices bends into the flow due

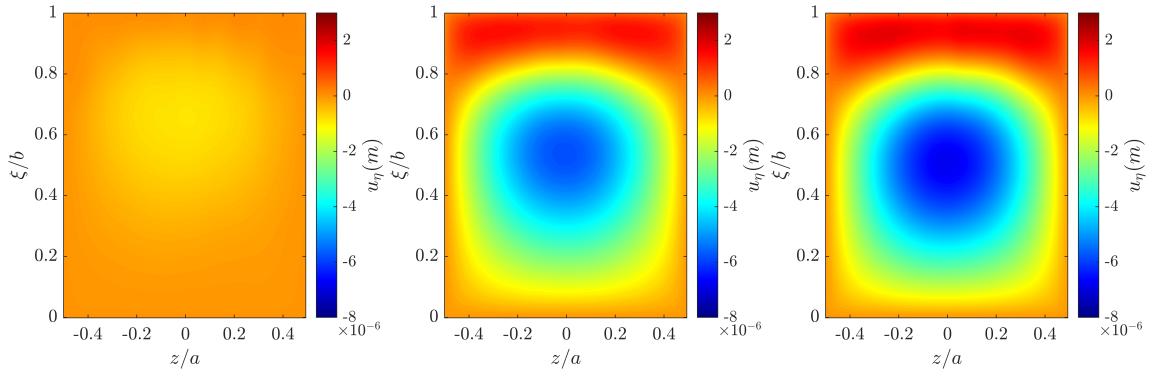

(a) t=1s **(b) t=30s** **(c) t=50s**

Fig. 13 Change in transverse displacement (u_η) due to panel heating, where a,b are the panel dimensions. Flow direction is from bottom ($\xi/b = 0$) to top ($\xi/b = 1$)

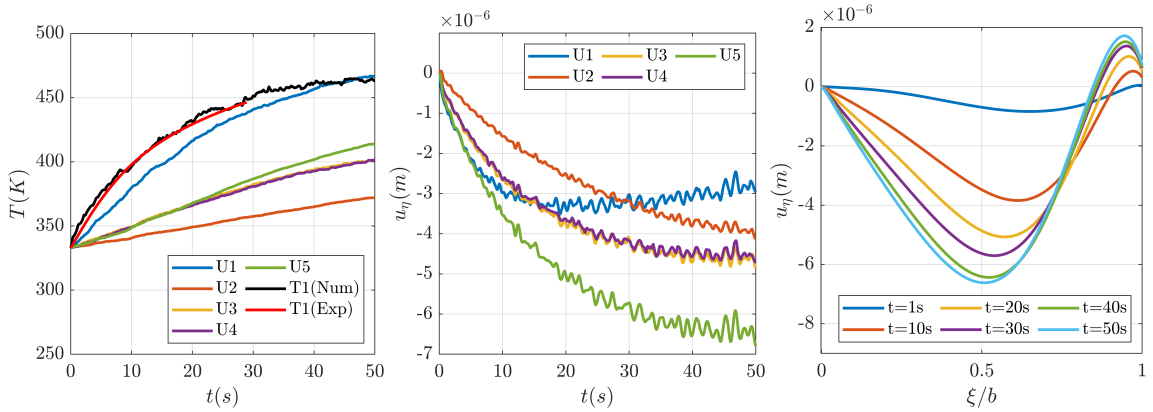

(a) Temperature rise **(b) Transverse displacement of the panel** **(c) Transverse displacement of the panel**

Fig. 14 Transient behavior of the compliant panel with the PSU Framework; Panel sensor location given in Fig. 1(b)

to thermal expansion. This phenomena is visualized with the u_η distribution across the centerline in Fig. 14(c). The change in transverse displacement across multiple sensor locations is given in Fig. 14(b). The panel midpoint 'U5' bends the most, up to $|u_\eta| = -6.5\mu$m away from the flow. The displacement distribution is symmetric across the centerline as inferred from probes 'U4' and 'U3' located at $\xi/b = 0.5, z/a = -0.02$ and $\xi/b = 0.5, z/a = 0.02$. The probe 'U2' at $\xi/b = 0.3, z/a = 0.0$ follows a similar trend but only displaces $u_\eta = -4\mu$m at the end of $t = 50$s. All the probes except the outlier 'U1' seem to reach equilibrium. Probe 'U1' located near the trailing edge at $\xi/b = 0.7, z/a = 0.0$ initially bends away from the flow, but as the thermal effects start to dominate, the slope changes direction at $t = 12$s. These results highlight the dominance of streamwise vortices on the thermal response of the panel.

2. USAFA Framework

The results discussed in this section are based off the coupled FTSI framework from Sec.III.C.3. Figure 15 illustrates the predicted temperature rise on the panel. Similar to the PSU Framework, the imprints of streamwise vortices are visible in Fig. 15(a). However, the predicted increase in temperature as seen in Fig. 15(b) and Fig. 15(c) is significantly higher than the PSU framework. This difference is attributed to the prediction of a higher heat load by the USAFA framework, especially with the reattachment streaks of streamwise vortices. This effect is not visible in the Stanton number comparison of Fig. 9 as the higher heat transfer values are clipped off to highlight features on the cone and slice sections. The difference in temperature rise is also attributed to the different treatments in the thermal boundary conditions between the two frameworks. The USAFA Framework has a more detailed contact modeling between the panel and the mounting frame, leading to a higher thermal resistance in the heat conduction. The temperature rise on the sensor locations of the panel is given in Fig. 16(a). Similar to the PSU Framework the temperature values reach an asymptotic behavior due to a reduction in the heat transfer. The corresponding transverse displacement on the five sensor locations is presented in Fig. 16(b). The panel displaces away from the flow which is associated with the dominance of fluid pressure on the top surface compared to the low cavity pressure on the bottom surface. Also note that the sensors 'U3' and 'U4', as shown in Fig. 1(b), are placed symmetrically w.r.t. the centerline, but the displacements are not symmetric. This is attributed to the fact that the structural mode shapes are asymmetric, which originates from the asymmetric placement of the thermocouple. The modal data will be analyzed in more details in the following section.

The observations derived from the FTSI prediction of both the frameworks are similar but elucidate mostly on the fluid-thermal interaction aspect. Therefore, a modal analysis is carried out in the next section to assess the change in the structural characteristics of the panel with increasing temperature.

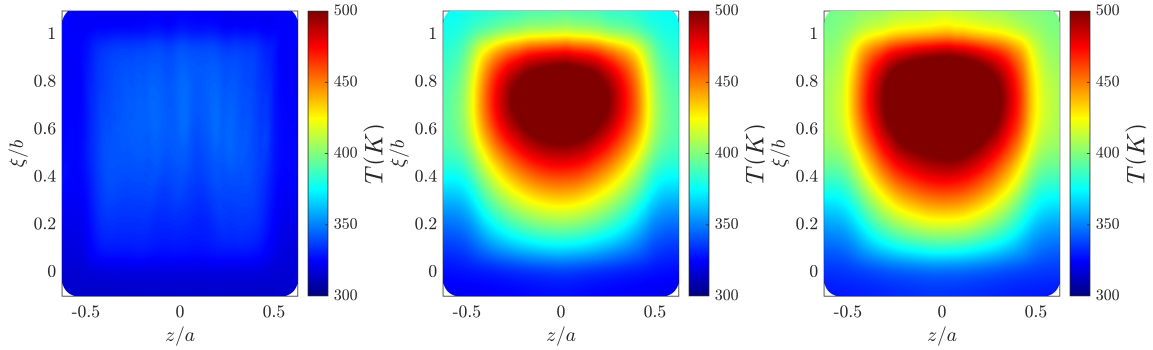

(a) t=1s **(b) t=30s** **(c) t=50s**

Fig. 15 Comparison of temperature distribution on the panel using coupled FTSI of USAFA Framework; Flow direction is from bottom ($\xi/b = 0$) to top ($\xi/b = 1$)

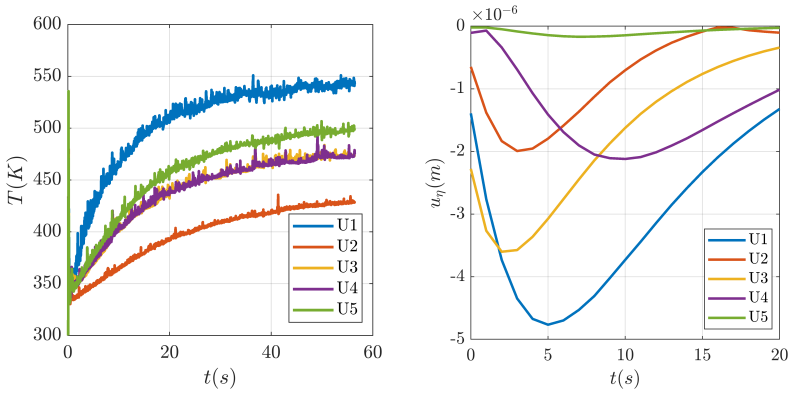

(a) Temperature rise **(b) Transverse displacement (u_η)**

Fig. 16 Transient behavior of the compliant panel predicted with the USAFA Framework.

B. Modal Analysis for Heated Panel

The modal content of the structure changes with varying surface temperature values [19–21]. In this case, the streamwise vortices contribute to the panel heating which in turn lead to the development of thermal stresses. The effect of temperature on the modal content of the panel is evaluated using the five accelerometers in the experiment, shown in Fig. 1(b) over a t = 20s runtime. The power spectral density (PSD) is computed with a Δt = 0.1s sliding window using the Welch method and normalized for each accelerometer. Then, these PSDs are combined and presented as a contour plot in Fig. 17. A SPOD analysis is performed on the initial t = 1.5s data of all five accelerometers to identify the mode shapes [19]. The first three modes correspond to (1,1),(1,2), and (2,1) in the increasing order of frequency as visible in Fig. 17. However, the peaks of modes (2,2) and (1,3) are not clearly distinguishable. They are spread over a broader peak centered around f = 17.5kHz. This discrepancy will be examined experimentally using LDV and DIC methods. Based on the present experimental data, three key observations are made: (1) The panel modal frequencies reduce with the increase in temperature. (2) The peak of mode (1,2) subsides around $t \sim$ 8s and energy is transferred to frequencies in the range 6-9kHz. (3) Mode (2,1) becomes stronger after $t \sim$ 2.5s. The physical reasons behind the phenomena 2 and 3 are yet to be determined when transient FSI analysis is performed at multiple time stations.

The numerical assessment for modal content of the panel is carried out using Rayleigh-Ritz (RR), also known as assumed mode method, and more refined FEM (Abaqus) discretely at time intervals of Δt = 5s. The non-uniform temperature distribution for computation of the thermal stress is obtained from the quasi-steady FTSI predictions of the PSU Framework. A discussion on the calibration of RR model is given in Sec.III.D. At t = 0s, the RR method is able to predict the frequencies of first three modes and fifth mode. However, with increasing panel temperature, the RR method consistently under predicts modal frequency of all the modes except the first one. Such a discrepancy is attributed to the differences in the temperature distribution, as the RR results are based on the FTI solutions that over-predict the temperature. The FEM model on the other hand accurately predicts modal frequencies for the first three modes with the effect of temperature rise. The predicted trend of fourth and fifth mode is consistent with the experimental data, but uncertainty in the identification of mode (2,2) and mode (1,3) frequencies restricts the assessment.

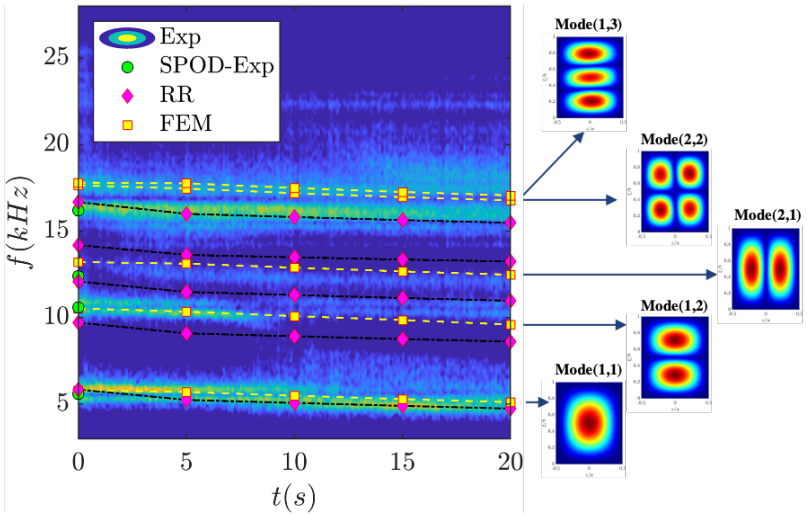

Fig. 17 Modal analysis of the panel (with sensors) to study the effect of temperature rise, with featured mode shapes obtained from FEM.

V. Transient Fluid-Structure Interaction

The transient FSI computation of the panel is conducted at the initial time instance of the FTSI analysis (around $t = 0$s) when the panel is undeformed and remains unheated. The predicted transverse displacement (u_η) of the panel from both the computational frameworks are evaluated and compared against the experimental data.

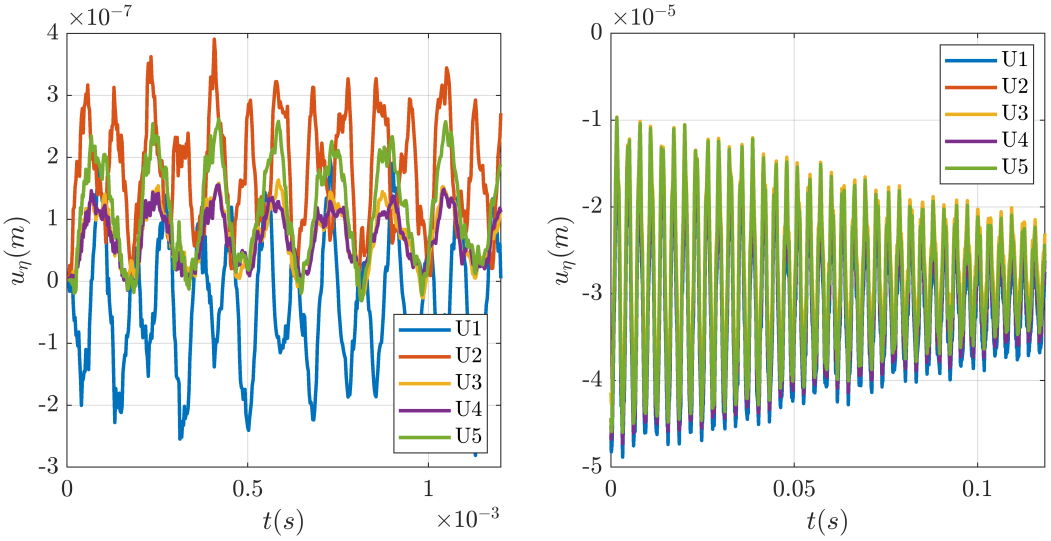

(a) Numerical(PSU) **(b) Numerical(USAFA)**

Fig. 18 Transverse displacement (u_ξ) of the panel around $t = 0$s; Sensor locations given in Fig. 1(b)

The u_η prediction from both the frameworks are compared in Fig. 18. The magnitude of u_η from the USAFA Framework is 10^2 higher than the PSU Framework. This is due to the initial excitation pulse in the structural solver of USAFA Framework. In the PSU Framework, u_η for 'U3 and 'U4' at $\xi/b = 0.5, z/a = -0.02$ and $\xi/b = 0.5, z/a = 0.02$ overlap depicting a symmetry in the displacement pattern across the centerline. The variation across streamwise direction is comparatively significant from the u_η values of 'U1','U2'and 'U5' at $\xi/b = [0.3, 0.7, 0.5], z/a = [0.0, 0.0, 0.0]$.

The panel dynamics are examined using the acceleration (a_η) solutions of both the numerical frameworks. The

acceleration is computed from the displacement u_η using the standard central difference scheme. A comparison of power spectral density (PSD) with the experimental accelerometer data is shown in Fig. 19 for all five locations. The PSD of a_η from the PSU Framework displays four distinct peaks at 5.8 ,10.7, 18.5, and 28 kHz consistently at all sensor locations. The frequency peak at 13kHz is only visible in the lateral sensor locations at 'U3' and 'U4' relating it to a spanwise mode. The first three peaks up to 13kHz reasonably match with the experimental data. It is observed that the experimental peak centered around 17.5kHz disperses over a broader range of frequencies from 16-18.5kHz. So, the fourth peak at 18.5kHz falls within the acceptable range. The PSD spectrum from USAFA Framework displays two peaks at 4.9kHz and 11 kHz. Note that the USAFA Framework uses projected modes for FSI computation obtained from the experimental hammer testing data. The occurrence of a_η peaks in the USAFA Framework is based on the excitation forces imparted by the unsteady aerodynamics. Further, it is important to identify the mode shape associated with each dominant frequency observed in the PSD.

The panel transverse displacement (u_η) computed from the PSU Framework is reconstructed in a reduced-order space using dynamic mode decomposition (DMD). The underlying theory for DMD is discussed in [34]. The computed frequency spectrum and eigenvalues are shown in Fig. 20. Dominant peaks in the frequency spectrum are annotated and their stability is assessed by plotting eigenvalues on a unit circle. Since, all the values lie on the unit circle, these modes are stable and oscillatory by nature. The DMD modes of the first six dominant frequencies are visualized in Fig. 21. These mode shapes are identified with the natural mode shapes of the panel. A dominance of streamwise direction modes is evident from the mode shapes. It also highlights the advantage of using numerical FSI to detect modal characteristics of the structure beyond the limitations of accelerometers in the experiment. In summary, the numerical FSI predictions match well with the experimental data validating the usage of present numerical frameworks for transient FSI analysis of the CSR structure.

The effect of structural response of the panel on the aerodynamic response is evaluated using the PSU Framework. The surface pressure data on panel from numerical FSI was compared against the rigid wedge case. Based on the numerical FSI predictions, the maximum panel displacement was about $|u_\eta| = 0.5\mu$m which is of the same order as the first grid size of fluid domain. The comparison of pressure data showed an insignificant contribution of structural displacement to the aerodynamics. Thus, it is inferred that CSR aerodynamic response is negligible for a panel with 1mm thickness under the present inflow conditions.

Based on the observations from FTSI and transient FSI results, a flow chart is presented in Fig. 22 illustrating the interaction amongst individual physical domains for the present study, where the thick arrows indicate the major interactional physics occuring in the current experimental setup. The aerodynamic heating causes temperature rise in the panel structure, and subsequently the structural deformation induced by the thermal stress. The transient structural response is excited by the aerodynamic pressure, but does not induce new flow structures in the flow field.

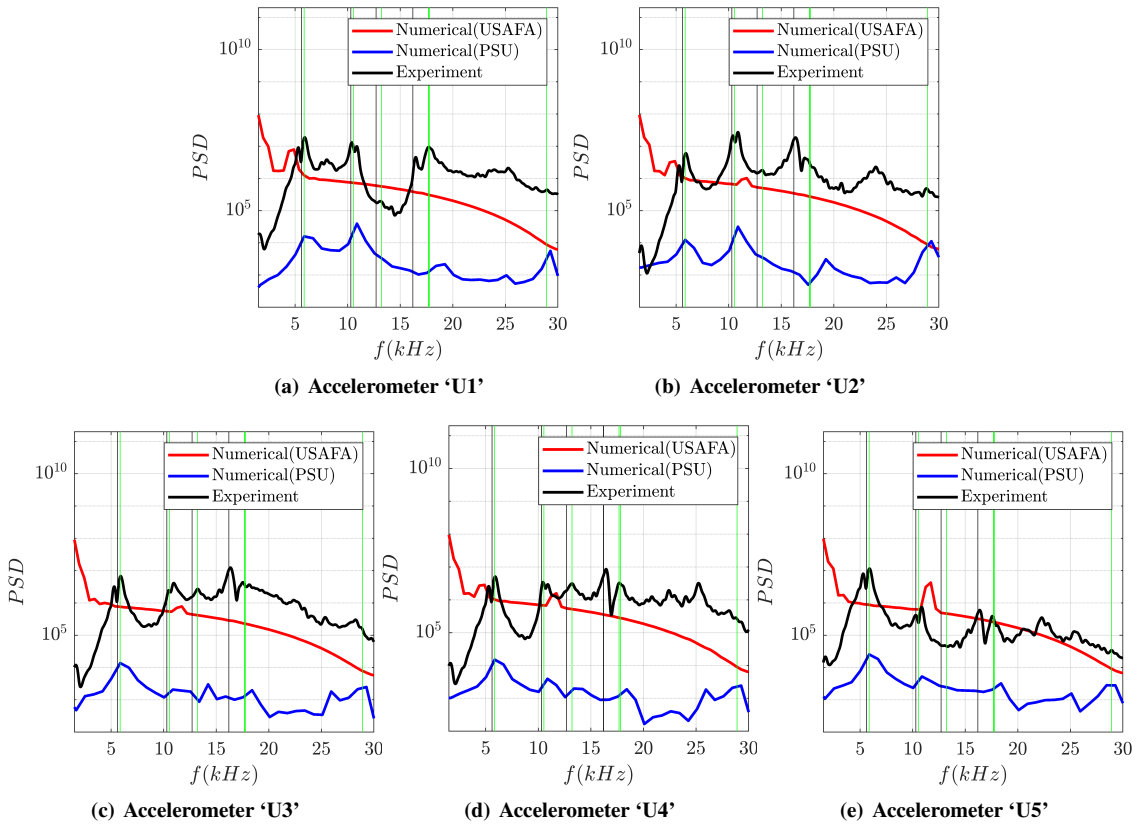

(a) Accelerometer 'U1' (b) Accelerometer 'U2'

(c) Accelerometer 'U3' (d) Accelerometer 'U4' (e) Accelerometer 'U5'

Fig. 19 Comparison of accelerometer PSD for the five sensor locations in Fig. 1(b); The PSD amplitude of Numerical(USAFA) has been reduced by a factor of 10^7 for comparison with the experimental data; Vertical green lines: Modal frequencies of the panel at [5.85, 10.53, 13.21, 17.68, 17.8, 28.9] kHz from Abaqus FEM; Vertical black lines: Modal frequencies of the panel at [5.6, 10.3, 12.7, 16.2] kHz from Experiment SPOD

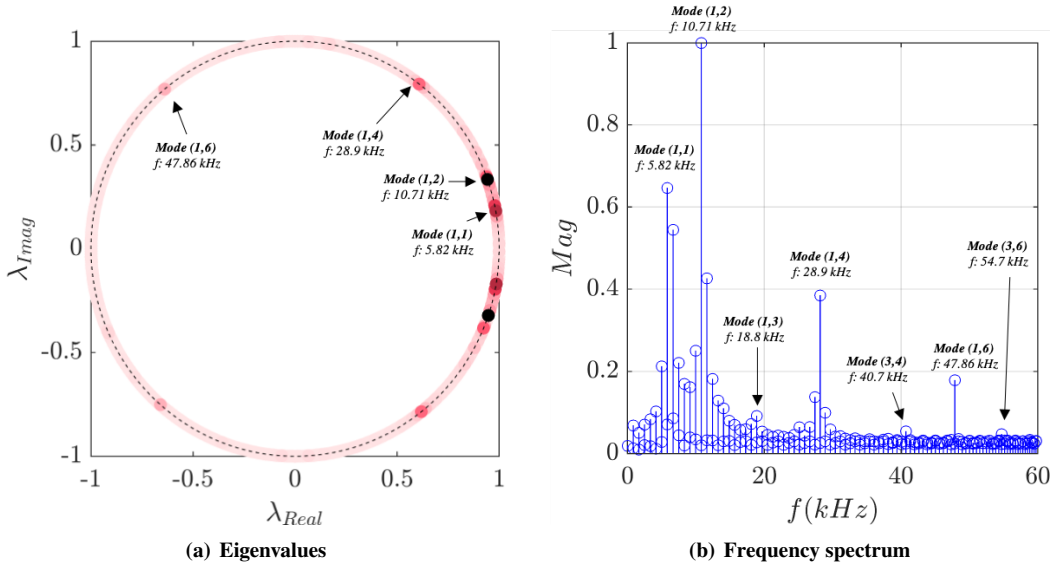

(a) Eigenvalues (b) Frequency spectrum

Fig. 20 Dynamic mode decomposition (DMD) of the transverse displacement (u_η) data from PSU Framework

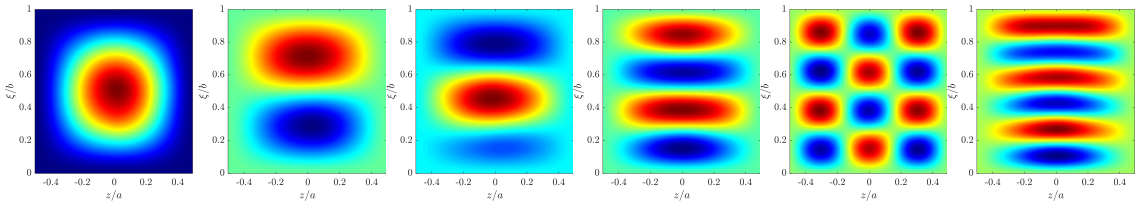

(a) Mode(1,1) (b) Mode(1,2) (c) Mode(1,3) (d) Mode(1,4) (e) Mode(3,4) (f) Mode(1,6)

Fig. 21 DMD mode shapes of the dominant frequencies based on transverse displacement (u_η) data from PSU Framework

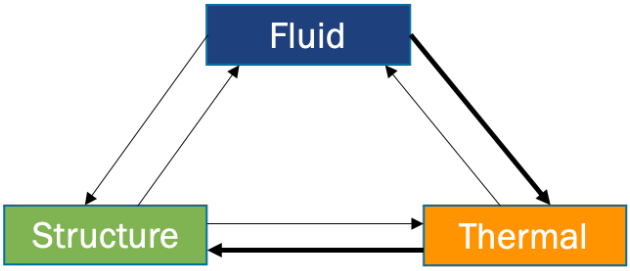

Fig. 22 Flow chart illustrating the FTSI for the present case with a 1 mm thick panel

VI. Conclusion

In this study, we have presented the computational FTSI analysis for a cone-slice-ramp geometry, and correlated the results with experimental data. Two laminar-solver-based computational frameworks, from PSU and USAFA respectively, are validated and compared. The PSU model considered the near field region of the CSR geometry with simplified structural model, while the USAFA model considered the entire test model, including the wake region and the internal structures. Both frameworks employed a decomposition strategy to compute the quasi-steady FTSI and transient FSI response separately. The main findings are the following,

1. Flow analysis of rigid panel case:
   (a) Both CFD solutions qualitatively capture the mean flow features, including the separation shock, shear layer impingement, and reattachment shock. The time-averaged solutions for aerodynamic pressure, heat transfer and wall shear stress match well with the experimental data.
   (b) For the time-resolved solution, the CFD results capture the main features of the experimental data, e.g. low frequency oscillation and shear layer flapping. But notable differences exist in the frequency spectrum due to limited time resolution.
   (c) Overall, the numerical solutions are shown to be effective for a more detailed resolution of the flow field, revealing flow features that are not easily observable in experiments, such as the upstream and downstream leg of streamwise vortices, and the origin of horseshoe and corner vortices. Both vortical structures contribute significantly to the aerodynamic heating.
2. Quasi-steady FTSI analysis over the entire period of experiment:
   (a) Panel displacement is mainly thermally driven due to the heat streaks of streamwise vortices. As a result, accurate prediction of heat flux is essential to correlate the computational FTSI response to the experiments.
   (b) A small magnitude of structural deformation in the order of 10^{-6}m is observed in the flow conditions considered, and such deformation has minimal impact on the flow field, esp. the heat flux. However, the aerodynamic heating does impact the structural modal properties and thus its deformation.
   (c) Numerical methods can reliably predict FTSI behavior of the structure beyond experimental runtime limitations, at least for the flow conditions considered in this study.
3. Transient FSI analysis of an unheated panel:
   (a) Due to the small structural deformation in the present study, the impact of the structural motion on the flow

field is minimal.

(b) Excitation of structural modes is mainly based on the frequencies overlapping with the unsteady flow structures. Therefore, it is critical to accurately predict the spectral contents of the flow field.

(c) Structural calibration is necessary for the validation of FSI results. In the present study, the importance of including sensor mass is shown for improving the accuracy of predicted modal frequencies, and hence the spectral contents in the predicted FSI response.

Based on the correlation between experimental and computational analysis, an assessment of the limitations of the computational frameworks is provided as follows,

1. The RANS-based analysis may not be able to accurately capture the localized transitional behavior in the laminar flow, e.g. in the post reattachment region of the current problem. The resolution of such flow features may further enhance the prediction of the flow spectral contents and thus the transient FSI responses. For future study, DNS/LES fluid solvers may be necessary to predict such transition behavior.
2. It is necessary to accurately describe the inlet boundary condition in the computational models so as to model the instability waves, which may also impact the transition characteristics and subsequently the spectral contents.
3. Further spatial and temporal resolutions may be necessary to capture the spectral content on the high frequency components, particularly the second mode waves. While the frequency of the second mode wave is much higher than the structural frequency, these waves may alter the transition characteristics in the flow field, leading to turbulent flow structures over the panel, which in turn may excite different structural responses.

Acknowledgments

Sandia National Laboratories is a multi-mission laboratory managed and operated by National Technology and Engineering Solutions of Sandia, LLC., a wholly owned subsidiary of Honeywell International, Inc., for the U.S. Department of Energy's National Nuclear Security Administration under contract DE-NA0003525. This work was in part supported by the High Performance Computing Research Center, HPCRC, at the United States Air Force Academy under contract FA7000-02-18-0011. The authors would like to acknowledge support of the DoD DSRC High Performance Computing Centers.

A. Rayleigh-Ritz Method

The Rayleigh-Ritz method is employed for the modal analysis of a nonuniformly-heated panel with added sensor masses. Since the panel is thin and its deformation is small, the classical thin plate theory is employed.

Consider a panel of side lengths a and b, thickness h, density ρ, Young's modulus E, Poisson's ratio ν, and thermal expansion coefficient α. The temperature distribution is $T(x, y)$ and assumed to be uniform throughout the panel. The material properties are assumed to be constant as the temperature rise in the experiment is limited. The sensors are approximated as point masses $\{m_i\}_{i=1}^{S}$, located at positions $\{(x_i, y_i)\}_{i=1}^{S}$.

The transverse displacement $w(x, y)$ of the panel is represented using a set of shape functions $\{\phi_{ij}(x, y)\}_{i,j=1}^{N}$,

$$w(x, y) = \sum_{i,j=1}^{N} q_{ij}\phi_{ij}(x, y) \equiv \boldsymbol{\phi}^T \mathbf{q} \tag{10}$$

where $\mathbf{q} = [q_{11}, q_{12}, \cdots, q_{NN}]^T$ are N^2 coefficients and $\boldsymbol{\phi} = [\phi_{11}(x, y), \phi_{12}(x, y), \cdots, \phi_{NN}(x, y)]^T$ are N^2 shape functions. In this study, for numerical stability, the Chebyshev polynomials are used,

$$\phi_{ij}(x, y) = T_i\left(\frac{2x - a}{a}\right) T_j\left(\frac{2y - b}{b}\right) \tag{11}$$

where $T_i(\eta) = \cos(n \arccos(\eta))$, $-1 \leq \eta \leq 1$.

The elastic energy due to bending is

$$\mathcal{U} = \frac{1}{2}\int_A \boldsymbol{\chi}^T \mathbf{D}\boldsymbol{\chi} dA \equiv \frac{1}{2}\mathbf{q}^T \mathbf{K}\mathbf{q} \tag{12}$$

where A represent the domain of the whole panel, and

$$\mathbf{D} = \frac{Eh^3}{1-\nu^2}\begin{bmatrix} 1 & \nu & 0 \\ \nu & 1 & 0 \\ 0 & 0 & \frac{1-\nu}{2} \end{bmatrix}, \quad \boldsymbol{\chi} = \begin{bmatrix} w_{xx} \\ w_{yy} \\ 2w_{xy} \end{bmatrix} = \begin{bmatrix} \boldsymbol{\phi}_{xx}^T \\ \boldsymbol{\phi}_{yy}^T \\ 2\boldsymbol{\phi}_{xy}^T \end{bmatrix} \mathbf{q} \tag{13}$$

The boundary conditions are applied using a penalty approach, which constrains the edges with extensional and torsional springs, with stiffnesses k_e and k_t. The corresponding elastic energy is

$$\mathcal{U}_c = \frac{1}{2}\oint_{\partial A}\left(k_e w^2 + k_t w_n^2\right) ds \equiv \frac{1}{2}\mathbf{q}^T \mathbf{K}_c \mathbf{q} \tag{14}$$

where ∂A denotes the boundary of the panel and w_n is the slope normal to the edge. Both k_e and k_t are set to be large numbers to enforce a clamped boundary condition.

The kinetic energy consists of contributions from the panel and the sensor masses

$$\mathcal{T} = \frac{1}{2}\int_A \rho h \dot{w}^2 dA + \frac{1}{2}\sum_{i=1}^{S} m_i \dot{w}(x_i, y_i)^2 \equiv \frac{1}{2}\dot{\mathbf{q}}^T \mathbf{M}\dot{\mathbf{q}} \tag{15}$$

The external work due to thermal stress is

$$\mathcal{W} = \frac{1}{2}\int_A \frac{E\alpha T}{1-\nu}(w_x^2 + w_y^2) dA \equiv \frac{1}{2}\mathbf{q}^T \mathbf{K}_T \mathbf{q} \tag{16}$$

Using the energy principles, from Eqs. (12)-(16), one may formulate a generalized eigenvalue problem,

$$(\mathbf{K} + \mathbf{K}_c - \mathbf{K}_T)\mathbf{u}_i = \omega_i^2 \mathbf{M}\mathbf{u}_i \tag{17}$$

where the ith mode shape of the panel is $\boldsymbol{\phi}^T \mathbf{u}_i$ with frequency ω_i. A convergence study is performed by increasing the number of shape functions. Eventually $N = 11$ is used, so that the errors in the frequencies of the first 4 modes are lower than 5%.

References

[1] Eason, T. G., Michael Spottswood, S., Chona, R., and Penmetsa, R., "A structures perspective on the challenges associated with analyzing a reusable hypersonic platform," *54th AIAA/ASME/ASCE/AHS/ASC Structures, Structural Dynamics, and Materials Conference*, 2013. doi:10.2514/6.2013-1747.

[2] Mcnamara, J. J., and Friedmann, P. P., "Aeroelastic and Aerothermoelastic Analysis in Hypersonic Flow: Past, Present, and Future," *AIAA J*, Vol. 49, No. 6, 2011. doi:10.2514/1.J050882.

[3] Daning Huang, "Development of a Hypersonic Aerothermoelastic Framework and Its Application to Flutter and Aerothermoelastic Scaling of Skin Panels," Ph.D. thesis, University of Michigan, Ann Arbor, MI, 2019.

[4] Gaitonde, D. V., "Progress in shock wave/boundary layer interactions," *Progress in Aerospace Sciences*, Vol. 72, 2015, pp. 80–99. doi:10.1016/j.paerosci.2014.09.002.

[5] Spottswood, S. M., Smarslok, B. P., Perez, R. A., Beberniss, T. J., Hagen, B. J., Riley, Z. B., Brouwer, K. R., and Ehrhardt, D. A., "Supersonic Aerothermoelastic Experiments of Aerospace Structures," *AIAA Journal*, Vol. 0, No. 0, 0, pp. 1–20. doi:10.2514/1.J060403.

[6] Riley, Z. B., Hagen, B., and Ehrhardt, D. A., "Aero-Optical Measurements of the Response of a Thin Panel at Mach 6," *AIAA Journal*, Vol. 0, No. 0, 0, pp. 1–15. doi:10.2514/1.J060408.

[7] Simeonides, A. N., G., and Haase, D. W., "Experimental and computational investigations of hypersonic flow about compression ramps," *Journal of Fluid Mechanics*, 1995, pp. 1–7. doi:10.1017/S0022112095002229.

[8] Navarro-Martinez, S., and Tutty, O. R., "Numerical simulation of Görtler vortices in hypersonic compression ramps," *Computers and Fluids*, Vol. 34, No. 2, 2005, pp. 225–247. doi:10.1016/j.compfluid.2004.05.002.

[9] Cao, S., Hao, J., Klioutchnikov, I., Olivier, H., and Wen, C.-Y., "Unsteady effects in a hypersonic compression ramp flow with laminar separation," *Journal of Fluid Mechanics*, Vol. 912, 2021. doi:10.1017/jfm.2020.1093.

[10] Butler, C. S., and Laurence, S. J., "Interaction of second-mode disturbances with an incipiently separated compression-corner flow," *Journal of Fluid Mechanics*, 2021, pp. 1–13. doi:10.1017/jfm.2021.91.

[11] Chuvakhov, P. V., and Radchenko, V. N., "Effect of Görtler-like vortices of various intensity on heat transfer in supersonic compression corner flows," *International Journal of Heat and Mass Transfer*, Vol. 150, 2020, p. 119310. doi:10.1016/j.ijheatmasstransfer.2020.119310.

[12] Roghelia, A., Chuvakhov, P. V., Olivier, H., and Egorov, I. V., "Experimental investigation of Görtler vortices in hypersonic ramp flows behind sharp and blunt leading edges," *47th AIAA Fluid Dynamics Conference*, 2017, pp. 1–14. doi:10.2514/6.2017-3463.

[13] McKiernan, G. R., "Instability and transition on a sliced cone with a finite-span compression ramp at Mach 6," Ph.D. thesis, Purdue university, 2020.

[14] Pandey, A., Casper, K. M., Spillers, R., Soehnel, M., and Spitzer, S., "Hypersonic shock wave–boundary-layer interaction on the control surface of a slender cone," *AIAA Scitech Forum*, 2020. doi:10.2514/6.2020-0815.

[15] Thome, J., Reinert, J. D., Dwivedi, A., and Candler, G. V., "Computational study of high speed flow on a sliced cone-flap geometry," *Fluid Dynamics Conference*, 2018, pp. 1–12. doi:10.2514/6.2018-3397.

[16] Terceros, M. J., and Araya, D. B., "Influence of boundary layer transition on the aerodynamics of a sliced cone with ramp at mach 6," *AIAA Scitech Forum*, 2021. doi:10.2514/6.2021-1852.

[17] Currao, G. M. D., Neely, A. J., Kennell, C. M., Gai, S. L., and Buttsworth, D. R., "Hypersonic Fluid–Structure Interaction on a Cantilevered Plate with Shock Impingement," *AIAA Journal*, Vol. 57, No. 11, 2019, pp. 4819–4834. doi:10.2514/1.j058375.

[18] Sullivan, B. T., Bodony, D. J., Whalen, T., and Laurence, S., "Direct Simulation of Fluid-Structure Interaction in Compression Ramp with Embedded Compliant Panel," *AIAA Journal*, Vol. 58, No. 11, 2020, pp. 1–45. doi:10.2514/1.J059072.

[19] Pandey, A., Casper, K. M., Soehnel, M., Spillers, R., Bhakta, R., and Beresh, S. J., "Hypersonic fluid-structure interaction on the control surface of a slender cone," *AIAA Scitech Forum*, 2021. doi:10.2514/6.2021-0909.

[20] Freydin, M., Levin, D., Dowell, E. H., Varigonda, S. V., and Narayanaswamy, V., "Natural frequencies of a heated plate: Theory and experiment," *AIAA Journal*, Vol. 58, No. 11, 2020, pp. 4969–4973. doi:10.2514/1.J059660.

[21] Whalen, T. J., Schöneich, A. G., Laurence, S. J., Sullivan, B. T., Bodony, D. J., Freydin, M., Dowell, E. H., and Buck, G. M., "Hypersonic fluid–structure interactions in compression corner shock-wave/boundary-layer interaction," *AIAA Journal*, Vol. 58, No. 9, 2020, pp. 4090–4105. doi:10.2514/1.J059152.

[22] Sadagopan, A., Huang, D., Xu, H. H. A., and Yang, X., "Numerical investigation of fluid-thermal-structure interaction for a control surface in hypersonic flow," *AIAA Scitech Forum*, 2021. doi:10.2514/6.2021-0911.

[23] Vasconcelos, P. B., McQuellin, L. P., Krishna, T., and Neely, A., *Experimental Study of Hypersonic Fluid-Structure Interactions on an Inclined Clamped-Free-Clamped-Free Compliant Panel*, ???? doi:10.2514/6.2021-4232.

[24] Oberkampf, W. L., and Aeschliman, D. P., "Joint computational/experimental aerodynamics research on a hypersonic vehicle. I - Experimental results," *AIAA Journal*, Vol. 30, No. 8, 1992, pp. 2000–2009. doi:10.2514/3.11172.

[25] Huang, D., Rokita, T., and Friedmann, P. P., "Integrated Aerothermoelastic Analysis Framework with Application to Skin Panels," *AIAA journal*, Vol. 56, No. 11, 2018, pp. 4562–4581.

[26] Luke, E., Tong, X., Wu, J., Tang, L., and Cinnella, P., "CHEM: A Chemically Reacting Flow Solver for Generalized Grids," *online document], URL: http://web. cse. msstate. edu/˜ luke/publications/CHEM_ AIAA2003. pdf [cited November 2016]*, 2003.

[27] "CHEM," `http://web.cse.msstate.edu/%7Eluke/chem/index.html`, last accessed Dec 2019.

[28] Toro, E. F., Spruce, M., and Speares, W., "Restoration of the contact surface in the HLL-Riemann solver," *Shock waves*, Vol. 4, No. 1, 1994, pp. 25–34.

[29] Luke, E., "Loci: A Deductive Framework for Graph-Based Algorithms," *Third International Symposium on Computing in Object-Oriented Parallel Environments*, edited by S. Matsuoka, R. Oldehoeft, and M. Tholburn, Springer-Verlag, 1999, pp. 142–153.

[30] Luke, E. A., Tong, X., Wu, J., Tang, L., and Cinnella, P., "A Step Towards 'Shape-Shifting' Algorithms: Reacting Flow Simulations Using Generalized Grids," *Proceedings of the 39th AIAA Aerospace Sciences Meeting and Exhibit*, AIAA, 2001.

[31] Luke, E., and George, T., "Loci: A Rule-Based Framework for Parallel Multidisciplinary Simulation Synthesis," *Journal of Functional Programming*, Vol. 14, No. 03, 2005, pp. 477–502.

[32] Jirasek, A., and Rizzi, A. W., "libm3l and lsipdx - Utilities for Inter-Process Data Transfer and Synchronization," *52nd Aerospace Sciences Meeting*, 2014. doi:10.2514/6.2014-1045.

[33] Dwivedi, A., Sidharth, G. S., Nichols, J. W., Candler, G. V., and Jovanović, M. R., "Reattachment streaks in hypersonic compression ramp flow: An input-output analysis," *Journal of Fluid Mechanics*, Vol. 880, 2019, pp. 113–135. doi: 10.1017/jfm.2019.702.

[34] Kutz, J. N., Brunton, S. L., Brunton, B. W., and Proctor, J. L., *Dynamic Mode Decomposition*, Society for Industrial and Applied Mathematics, Philadelphia, PA, 2016. doi:10.1137/1.9781611974508.